Laser-assisted synthesis of carbon coatings with cobalt oxide nanoparticles embedded in gradient of composition and sizes

Mihai Sopronyi, Cristina Nita, Jean-Marc Le Meins, Loïc Vidal, Florin Jipa, Emanuel Axente, Camélia Matei Ghimbeu, Felix Sima

To cite this version:

Mihai Sopronyi, Cristina Nita, Jean-Marc Le Meins, Loïc Vidal, Florin Jipa, et al.. Laser-assisted synthesis of carbon coatings with cobalt oxide nanoparticles embedded in gradient of composition and sizes. Surface and Coatings Technology, 2021, 419, pp.127301. ⟨10.1016/j.surfcoat.2021.127301⟩. ⟨hal-03445290⟩

HAL Id: hal-03445290
https://hal.science/hal-03445290v1

Submitted on 13 Jun 2023

Version of Record: https://www.sciencedirect.com/science/article/pii/S0257897221004758
Manuscript_58b8f2c92c3ef38176dde86008ce3e05

Laser-assisted synthesis of carbon coatings with cobalt oxide nanoparticles embedded in gradient of composition and sizes

Mihai Sopronyi[a], Cristina Nita[a], Jean-Marc Le Meins[b,c], Loïc Vidal[b,c], Florin Jipa[a], Emanuel Axente[a,*], Camélia Matei Ghimbeu[b,c,*] and Felix Sima[a]

[a]National Institute for Laser, Plasma and Radiation Physics, 077125 Magurele, Romania;

[b]Université de Haute-Alsace, Institut de Science des Matériaux de Mulhouse (IS2M), CNRS UMR 7361, F-68100 Mulhouse, France.

[c]Université de Strasbourg, F-67081 Strasbourg, France

*Corresponding authors: camelia.ghimbeu@uha.fr. (C. Matei Ghimbeu), emanuel.axente@inflpr.ro. (E. Axente)

Abstract

We report on a new laser-assisted method for the synthesis of composite coatings consisting of cobalt oxide-embedded porous carbon with gradient of composition and sizes. Uniform carbon thin films containing cobalt oxide nanoparticles (CoO NPs) of various concentrations and sizes are obtained by Combinatorial Matrix-Assisted Pulsed Laser Evaporation (C-MAPLE) followed by a post-annealing treatment. Specifically, simultaneous pulsed laser irradiation of two concentric cryogenic targets was applied for gradient thin films assembling on solid substrates. Both targets contained environmentally friendly phloroglucinol/glyoxylic acid organic precursors and a template dissolved in an ethanol-chloroform mixture, whereas one of them enclosed, in addition, cobalt nitrate salt. Due to angular dispersion and crossing of the two vapor plumes during co-deposition process, thin composite polymeric nanocoatings containing Co nitrate salt were obtained. After subsequent thermal annealing treatment of samples at 600^{o}C, mesoporous carbon films exhibiting CoO NPs gradient distribution were then directly obtained onto the substrates. Carbon matrix formation was supported by EDX analyses and characteristic D, G and 2D bands present in the Raman spectra. Co NPs concentration varied from 3 to 32 *wt%* on the substrates with a minimum at furthest interaction point of the Co salt containing plume and substrate, while carbon concentration significantly decreases from 91 to 63 *wt%*. Oxygen amount was relatively constant at about 6 *wt%* for all coatings. The CoO NPs are homogenously dispersed in the carbon matrix whereas a tendency for aggregation is observed for high loadings. In addition, ~~homogeneous the~~ CoO NPs ~~dispersion within carbon matrix was further evidenced while the~~ size gradient distribution ranged from 3 to 8 nm with the minimum size correlating the minimum concentration.

Keywords: mesoporous carbon; CoO nanoparticles; combinatorial laser-assisted deposition; thin films, variable composition.

1. Introduction

During the last years, research has been focused to develop new carbon-based nanomaterials suitable for a wide range of applications. Due to its high specific surface area and large pore volume, tunable pore sizes and architectures, pore connectivity and the possibility to be decorated with different chemical species (N, S, O atoms or metallic/metal oxides particles), the mesoporous carbon materials stood out as high performing potential candidate for energy conversion and storage [1], catalysis [2], sensing [3], adsorption [4,5] and biomedical applications [6,7].

Since its positive impact on the development of various research fields was proven, studies were performed to find new strategies to obtain mesoporous carbon. The first approach proposed in the literature is the *hard-template* [8,9] which allows the successful fabrication of mesoporous carbon materials with high specific surface area and interconnected porosity. However, the multi-step procedure, hazardous chemical pathways and high cost represent significant inconvenient of this method. As an alternative, a *soft-template* approach [10], with reduced synthesis steps and the possibility to obtain high amount of material per synthesis [11] was proposed to overcome a part of the drawbacks of *hard-template* approach. Some limitations such as the use of formaldehyde as a cross-linker in the phenolic resin formation, known to be a carcinogen compound, concentrated acids in high-temperature or high-pressure conditions, are still encountered in the case of the *soft-template* approach. In this context, finding a convenient synthesis method to obtain mesoporous carbon materials is still of great interest.

A green *soft-template* approach using the self-assembly of environmentally friendly phloroglucinol/glyoxylic acid carbon precursors at room temperature was proposed by our group [10]. This served as basis for further studies aimed at finding simple and eco-friendly methods to obtain mesoporous carbon materials. Moreover, the carbon-based materials synthesized by this evaporation induced self-assembly approach (EISA) have successfully served as support for different type of nanoparticles (NPs), allowing the formation of hybrid materials with improved properties for the targeted application [12–16]. Even if this synthesis protocol is much simpler compared to the conventional *hard* and *soft template* approaches, long thermal treatments at high temperatures are still necessary to obtain the mesoporous carbon.

Previous studies proposed a time-efficient light-assisted evaporation induced self-assembly (LA-EISA) approach involving a short-time UV laser irradiation of the carbon precursor solution which avoids the long-time thermal polymerization step and allows a good control of the carbon porosity by tuning the irradiation conditions [1,17]. Moreover, an improvement of mesoporous carbons properties was achieved through different doping methods as e.g. with heteroatoms (B, P, N [18–22]), different metals and metal oxides (Pd, Pt, Ni, Ru, Cu, Sn, Sb, Co, SnO_2, SiO_2 [23–27], and alloys (Pt/Ru, Pt/Co, Ni/Fe, Ni/Co [12,28,29]). We have shown that LA-EISA could be successfully applied for the synthesis of porous carbon with embedded magnetic cobalt nanoparticles [17]. The influence of three metallic Co salts precursors (acetate, nitrate, and chloride) on both the phenolic resin and carbon characteristics (structure, texture, and particle size/distribution) was demonstrated. Thus, cobalt acetate and nitrate salts revealed the formation of very small (3 ÷ 6 nm) and uniformly dispersed particles that are superparamagnetic, while cobalt chloride precursor induced the formation of large and heterogeneously poly-dispersed particles in the carbon matrix that exhibits ferromagnetic properties [17]. However, most of the approaches depicted before allows the direct synthesis of carbon nanostructures in powder-like form only.

More recently, an improvement of the LA-EISA approach was proposed by using Matrix-Assisted Pulsed Laser Evaporation (MAPLE) technique [30], for the synthesis of porous carbon thin films. This deposition technique proved suitable to grow high quality thin films of a wide range of materials both organic and inorganic [31–34]. Porous carbon thin films were obtained by applying MAPLE to a cryogenic target of phloroglucinol/glyoxylic acid carbon precursors dissolved in organic solvents, followed by a thermal carbonization step. Kr adsorption/desorption analyses revealed the formation of interconnected mesoporous structures, with pore sizes between 10 to 15 nm, uniformly distributed inside carbon coatings [30]. Two main advantages of the MAPLE method can be enlisted: (i) the possibility to replace the thermo-polymerization step and thus reduce the processing time and (ii) the good control of the textural and morphological properties by modifying the laser irradiation parameters or target solvents.

In the present study, we report on a new approach for synthesis of mesoporous carbon thin films with CoO NPs embedded in gradient of both concentration and sizes by Combinatorial Matrix-Assisted Pulsed Laser Evaporation (C-MAPLE) method. C-MAPLE is a single-step laser-assisted approach which generally allows to create a compositional gradient of two compounds on various substrates during simultaneous laser co-evaporation of two cryogenic targets and thin-film co-deposition process [35]. The main advantage of this method represents the possibility to use any two different compounds to generate a combinatorial library and consequently to create new materials or innovative properties [35]. Here, we demonstrate the possibility to obtain compositional gradient composite coatings consisting in CoO NPs embedded in a carbon matrix.

2. Materials and Methods

2.1. Chemicals

The materials used for the experiments are: triblock copolymer Pluronic F127 (poly(ethylene oxide)-block-poly (propylene oxide)-block-poly- (ethylene oxide, $PEO_{106}PPO_{70}PEO_{106}$, M_w = 12 600 Da), phloroglucinol (1,3,5-benzenetriol, $C_6H_6O_3$), glyoxylic acid monohydrate ($C_2H_2O_3 \cdot H_2O$), cobalt(II) nitrate hexahydrate ($Co(NO_3)_2 \cdot 6H_2O$), ethanol absolute (C_2H_5OH) and chloroform ($CHCl_3$) from Sigma-Aldrich.

2.2. Thin films synthesis approach

C-MAPLE experiments are carried out inside a stainless-steel reaction chamber (Figure 1.a) in which a specific irradiation geometry and alignment is achieved before deposition. In the following, several experimental steps are performed as e.g.: targets and substrates preparation, optimization of the deposition conditions (energy balance, laser spots size, dynamic pressure, repetition rate of the laser, and number of pulses to be applied) and finally the films growth, as detailed in our previous studies [34,35].

Targets preparation. The targets consist of two distinct solutions: one containing Co nitrate salt (S_{CoX}) and the other without (S_0). The S_0 solution is prepared by mixing the carbon precursors (phloroglucinol/glyoxylic acid) and the template (Pluronic F127) with solvents using the constituents-solvent ratio proposed in our previous work [17,30]: Pluronic F127 – 2 g; phloroglucinol – 1 g; glyoxylic acid – 0.75 g; ethanol – 25 ml; chloroform – 25 ml, over which 0.5 g Co(II) nitrate salt is added to obtain the S_{CoX} solution. We selected these solvents based on our previous studies, in order to preserve the chemical composition of the targets [30]. The solutions were poured in a target holder consisting of two separate ring-shaped vessels, as follows: 5 ml of S_{CoX} - in the inner ring and 8 ml of S_0 - in the outer ring (Figure 1.b). The holder was further immersed in liquid nitrogen for 30 minutes for solidification. A digital photograph of the cryogenic targets assembling is presented in Figure S1.a [of the Supplementary Information (SI) section], where the carbon precursors solution is colorless, while the addition of cobalt nitrate salt changes its color to pinkish.

Substrates preparation. The substrates used for these experiments were 10×10 mm^2 cut Silicon. They were cleaned for 15 min in successive ultrasonic baths of acetone, alcohol, and distillated water, then dried with high purity N_2. The cleaning was followed by plasma etching for 5 min on each side of the substrates, in a flow of O_2 at 20 SCCM, at a radio-frequency power of 80 W at 40 kHz. Afterwards, the substrates were mounted on a substrate holder. For easy monitoring (Figure 1.b), they were denominated from left to right as S1 to S5, while facing the S_0 and S_{CoX} targets respectively. The substrate holder was then placed inside the reaction chamber, facing the target holder, at a separation distance of 5 cm.

Experimental setup. An UV KrF* excimer laser (Lambda Physics Coherent, COMPexPro 205, λ=248 nm, τ_{FWHM} = 25 ns) was used for thin films deposition. The laser beam was split (Figure 1.a) and focused onto the targets. After optimization, the laser fluence of the beams were set to 2.7 J cm^{-2} for $S_{CoX;}$ and 1.5 J cm^{-2} for S_0 to obtain coatings with rather uniform thickness (~700 nm, as measured on the phenolic resin sample S3, in the middle of the compositional library – see Figure S2 in SI). Two distinct regions from the two targets are thus simultaneously irradiated, evaporating at the same time both materials, which are further collected on the facing substrates generating the gradient coatings (Figure 1.b). The substrates were kept fixed, while the cryogenic targets were rotated at 50 rpm to avoid drilling, and continuously supplied with liquid nitrogen. 6000 subsequent laser pulses at a repetition rate of 5 Hz were applied in a dynamic pressure of 2×10^{-2} mbar to obtain the compositional gradient thin films. Images of the cryogenic targets at the end of C-MAPLE experiments as well as of the gradient coatings are presented in Figures S1.b-c, revealing a color change to orange, as a clear evidence of photo-polymerization and self-assembling. Finally, the polymeric thin films were subjected to a carbonization step, in inert Ar atmosphere for 1 hour, at 600°C, with a heating ramp of 2°C/min, resulting in dark carbon coatings (see Figure S1.d).

2.3. Materials characterization

Surface nano-features and CoO NPs sizes were investigated with a JEOL ARM-200F transmission electron microscope (TEM) working at 200 kV. The chemical composition of the coatings was determined by EDX mapping (coupled to Scanning-TEM) with a JED 2300 detector. Complementary microstructure analysis was performed by Raman spectroscopy in a backscattering geometry using a LabRAM BX40 (Horiba Jobin-Yvon) micro-spectrometer equipped with a diode pumped solid-state laser excitation source (Compass 315M-50, λ = 532 nm). The crystalline structure of the materials was investigated by grazing incidence α_i = 1°

X-ray diffraction (GI-XRD) using a powder diffractometer D8 ADVANCE A25 from Bruker. The experimental setup is equipped with a parabolic 60 mm Goëbel mirror and a line focus Cu K$\alpha_{1,2}$ radiation tube (40 kV/40 mA). The parallel incident X-ray beam was collimated with 0.02 mm primary slits. The sample is mounted on a UMC XYZ motorized stage. For this incident angle, the footprint of the X-ray beam does not exceed the length of the sample. The diffraction data are collected on a high-resolution energy dispersive 1-D detector (LynxEye XE-T) in front of which equatorial 0.02° Soller slit is positioned. Data collection is ranging from 20 up to 60°2θ with a step size of 0.04°2θ for a total counting time of 16h. Coherent diffraction domain size was calculated from the full width at half maximum intensity (FWHM) assuming no other microstructural effects, and using Scherrer equation [36]. Image J software was used to determine the particle size distribution by counting between 250 and 2700 particles, depending on the density of population on each material. Surface morphology was investigated by high-resolution scanning electron microscopy (HR-SEM) using a JEOL JSM-7900F. Thickness evaluation was performed by atomic force microscopy (AFM) using a TT-AFM Workshop microscope operated in tapping mode on 15×15 μm^2 regions under ambient conditions. A representative example is given for the phenolic resin sample S3 (before the carbonization step), in the middle of the gradient coatings (Figure S2 in SI). The measurement was performed on sample with a step, the thickness being determined from the horizontal height profile to be about 700 nm.

3. Results

3.1. Energy-dispersive X-rays spectroscopy

Nanoscale insights about the gradient composite coatings are achieved by EDX coupled with STEM imaging. High-resolution elemental mapping evidenced the presence of C, Co and O in all samples, as seen in the representative images of Figure 2, acquired on sample S2. Moreover, although uniformly distributed, Co is mostly concentrated in the regions of the brighter spherical spots embedded in a grayish matrix observed in the corresponding STEM mapping (upper left image). These bright regions (STEM) overlaps with the yellow regions from the EDX mapping confirming the Co presence. Here, the matrix is mostly composed by uniformly distributed C and O, but without exhibiting a certain level of structural organization.

~~Quantitative~~ EDX-TEM analysis allows the evaluation of average Co, C and O mass fractions in each sample of the gradient coatings. The measurements were performed in several distinct regions on the surface of each sample, the results being averaged. The data collected in Table I reveals rather an exponential increase of Co concentration along the longitudinal direction of the compositional library from about 3 *wt%* to 32 *wt%* (0.74 ÷ 9.1 *at%*) and demonstrate the Co gradient formation (see also EDX spectra in Figure S3 of the SI for details). In the same time, the amount of carbon significantly decreases from about 91 *wt%* to 63 *wt%* (94.7 ÷ 85.7 *at%*) in the films. The oxygen level (~ 6 *wt%* / between 4.57 ÷ 5.17 *at%*) seems to vary only a slightly among the samples. For more clarity elemental distribution presentation, a graphical representation of the mass fractions variation along the longitudinal direction of the gradient is presented in Figure 3. To explain the evolution of chemical composition within the films, a hypothesis where two factors that are systematically competing can be proposed. First, it should be mentioned that oxygen is bonded on the carbon surface in form of oxygen functional groups as reported previously [37] ~~and~~ but also bonded on Co in form of CoO (as will be shown by XRD and Raman spectroscopy) ~~low, probably as a thin layer on the surface of the material. Secondly, the smaller particles are more prompted to be oxidized.~~ As the C and Co amounts varies oppositely within the series S1 to S5, i.e., C decrease whereas Co increases, the O amount remains rather stable. However, the limitation of EDX techniques in terms of light elements (C and O) quantifications should be as well considered. Nevertheless, complementary analyses techniques such as X-ray photoelectron spectroscopy (XPS) must be employed to confirm the evolution of O-C and O-Co bonds and the proposed hypothesis.

~~Therefore, for rich carbon composition in the films (S1-S2), the O coming from the functional groups is high and the amount bonded to Co is low, while for poor composition in carbon (S4-S5), the overall oxygen amount bonded to carbon will decrease in the favor of oxygen bonded on Co. This may explain the rather smooth variation of oxygen level in the materials.~~

3.2. Raman spectroscopy

The microstructure of the obtained mesoporous carbon/CoO composite thin films was determined by Raman analysis. All the samples (Figure 4.a) confirm the formation of carbon, by the presence of two specific peaks: D (defect band) and G (graphite band). The spectra were recorded in the 3500-250 cm^{-1} region and normalized to G band. The peak at 1330 cm^{-1} is associated to the D band and represents the breathing mode of sp^2 hybridized carbon rings activated adjacent to a defect. The one at 1580 cm^{-1} represents the G band, which correlates to the in-plane vibration of the sp^2 bonded carbon atoms. The analyses revealed that the intensity of D band increases along the gradient (S1 to S5), with the decrease of the amount of carbon (Figure S4 in SI). Modification of the peaks FWHM (full-width at half maximum) are observed as well. For non-graphitic materials, the ratio $FWHM_D/FWHM_G$, is recommended to be used [38] to estimate the degree of disorder. The obtained values are rather constant (~ 2.6) (table inset in Figure 4.a), for coatings having high amount of carbon (90.7 to 85 *wt%*, S1 to S3) and their high values suggest rather disordered-like materials. These values smoothly decrease (from 2.56 to 2.24) for coatings containing lower amounts of carbon (85 to 62.5 *wt%*, S3 to S5). At a first glance, this would suggest a slight increase in the carbon organization, although the significant differences in the composite composition (different amount of carbon) and coating films should not be neglected. Moreover, spectra evidenced the presence of 2D band located at 2900 cm^{-1}, which is typically characteristic to graphitic domains in the carbon microstructures. Their broad and undefined shape, sustain as well the disordered nature of the carbons [38]. The same evolution is shown for 2D band intensity, in line with the D band. Other additional peaks can be observed, located at 457, 504 and 660 cm^{-}

^{1} (Figure 4.b.) and associated with the E_g, T_{2g} and A_{1g} modes ~~presence~~ of cubic CoO ~~oxides~~ [39,40], in agreement with other recent studies [41]. Indeed, a lower temperature used for carbonization (600°C) could lead to insufficient reduction of CoO to Co NPs. CoO could be also formed due to superficial oxidation of metallic nanoparticles, as a consequence of thin films exposure to ambient atmosphere [42].

3.3. Grazing incidence X-ray diffraction analyses

The X-ray diffraction patterns recorded on S1 – S5 coatings are presented in Figure 5.a. They clearly identify the broad peaks between 20-27° as the (002) reflection planes of graphite, indicating disordered-like materials with a low graphitization level of the carbon coatings. The presence of CoO NPs inside an amorphous carbon matrix was confirmed by GI-XRD investigations. Diffraction patterns recorded for samples S3 to S5 revealed, even if diffraction data remain a little noisy, increasing CoO peaks (COD 1541662 [43], in agreement with Raman analyses. Indeed, the presence of (111) and (200) reflection planes revealed the formation of face-centered-cubic phase of cobalt monoxide nanostructures [44]. Zhou et al. [45] also reported the formation of composite of CoO - amorphous carbon matrix, during synthesis of cobalt nanoparticles supported on nitrogen-doped porous carbon nanowires at calcination temperatures below 600°C due to incomplete carbonization and reduction. Indeed, at this temperature many oxygen functional groups are still present on the materials as indicated by the oxygen content (Table I) and EDX mapping which hinder the complete reduction of the particles.

The (200) reflection, which is the most intense, was selected for an individual profile fitting using WinPlotr software [46]. Data where initially converted into suitable format via PowDLL [47]. According to the assumptions of Scherrer's formula, Gaussian profile shape was selected (Figure 5.b). The results led us to get some basic information about intensities and FWHM evolutions with initial CoO% in the synthesis (for S3, S4 and S5). Main results are summarized in Table II. Even if the estimated standard deviation is quite important

(Figure S5.a in SI section), especially for S3, data analyses evidenced an increase of diffraction peaks intensity with CoO content within coatings. At the same time, the FWHM of the CoO (200) reflection decrease (see Table II), corresponding to an increase in the size of the coherent diffraction domains, supposing that only size-effects influence lines broadening or are dominant. Coherent diffraction domain sizes were calculated from the FWHM using Scherrer equation, considering the errors related to line position and FWHM issued from profile refinement (Figure S5.b). A progressive increase of crystallite size from 2.6 nm to 8.0 nm and 9.6 nm is observed from S3 to S5 films. Indeed, in a previous study [17], we have shown that cobalt precursor salts (acetate, nitrate, chloride) have a high influence on the crystallites size, as evaluated from XRD patterns. LA-EISA of nitrate salt solutions revealed the formation of about 4 nm Co NPs embedded in a mesoporous carbon matrix, in good agreement with the present study, for the same amount of Co in the materials corresponding to sample S3.

3.4. Transmission Electron Microscopy

TEM analysis of the gradient coatings is presented in Figures 6.a-e, and evidence the presence of CoO particles. These could be identified as dark quasi-spherical shapes embedded in a grey carbon matrix. The particles are rather uniformly dispersed throughout carbon network for low concentration of CoO (< 10 at. % Co) whereas for larger concentration, a slight tendency of particle agglomeration is observed (Fig. 6d-e).

Very uniform and continuous porous carbon thin films could be noticed, in good agreement with our previous study using classical MAPLE of polymers only [30], developed in similar experimental conditions (the same solvent mixture 1 : 1 - C_2H_5OH : $CHCl_3$ for target preparation and rather similar UV irradiation dozes).

However, particles seem to influence carbon ordering, studies suggesting that salts have a distinct effect on the materials self-assembly by modifying both the size and the shape of micelles [17]. The right column in the figure is devoted to particles analyses. CoO NPs size distribution evidence a gradual increase from sample S1 to S5, from about 3 to 8 nm (see Table II). Here, the measurements were performed in several distinct zones on the surface of each sample, and the counted particles were compiled as particle size diagrams, allowing the determination of mean particle size. Moreover, one can observe an increase in CoO NPs density along the longitudinal direction of the gradient coatings (last column in Table II). The number of particles increase almost linear up to 10 times, from one side to another in our experimental conditions for combinatorial coatings synthesis, in perfect agreement with particles mass increase determined by EDX. Indeed, experimental data fitting of size distribution with a lognormal function (see last column in Figure 6) evidenced a clear broadening effect, in agreement with the evolution of CoO NPs concentration.

Furthermore, with increasing the CoO NPs quantity and density, larger particles are formed, most probably by the agglomeration of small clusters (samples S4-S5 in Figures 6.d and e). This phenomena of increase of particle size is known as Oswald ripening mechanism [48]. Smaller particles are less thermodynamically stable and they have tendency to attract other neighbor particles to form larger and more stable particles. Indeed, at high concentration of particles the neighbor particles are placed much closer favoring their interaction and growth. These observations are in good agreement with the analyses presented before. Indeed, both GI-XRD and EDX revealed the successful formation of ~~uniformly distributed~~ a gradient CoO NPs in mesoporous carbon coatings while their sizes, ~~and~~ concentrations and aggregation gradually increase.

Selected area electron diffraction (SAED) has been performed on S2 and S5 samples to get insights on the crystallinity (Figure 7). For S2 sample (Fig. 7.a), three diffuse diffraction rings are observed, while for S5 (Fig. 7.b) three well defined rings and several diffuse ones are seen. This indicated a higher crystallinity in the case of S5 material, in agreement with the XRD and Raman results. The measurement of the interlayer spaces (*d*) allows to identify for S2 the rings corresponding to (111), (200) and (202) diffraction planes of crystalized CoO. For S5, in addition, the diffraction plans related to (311), (222), (400) and (402) are observed, in line with XRD diffractograms and COD 1541662 of cubic CoO.

The evolution of most common nanoparticle's sizes with respect to their average mass percentage determined for each sample of the gradient coatings is presented in Figure 8. One could notice an apparently exponential increase of this ratio from S1 to S5 in agreement the average CoO NPs counted after TEM analyses. This distribution could be correlated with the expansion of the evaporated fluxes of the two plumes. Most of the materials on substrates are collected perpendicular to the region where the laser beam interacts with the cryogenic target. Here, the cobalt nitrate salt precursor starts to agglomerate due to higher density of expulsed material leading eventually to slightly larger nanoparticle clustering as seen in the S3-S5 regions of the coatings. ~~Nonetheless, independent on their sizes, all the nanoparticles are uniformly dispersed all over the coatings.~~

3.5. High-resolution Scanning Electron Microscopy

More insights on the surface morphology of the coatings were assessed by HR-SEM investigations (Figure 9). Analyses reveal that the CoO NPs are uniformly distributed throughout the mesoporous carbon gradient thin films, in agreement with previous EDX and STEM analyses. A representative example is given for the sample S3, in the middle of the compositional library. Here CoO NPs are shown as light-grey quasi-spherical structures embedded in a darker carbon matrix. The network looks uniform, no sign of cracks or peelings being observed all over the gradient coatings. Moreover, the analysis also confirms our previous TEM observation and shows that the larger CoO NPs are formed (on S3 to S5 coatings) by the agglomeration of smaller ones as sub-micrometer clusters. This is evidenced in the higher magnification image of Figure 9 (right 25.000 ×), where CoO NPs start clustering as quasi-uniform round structures uniformly distributed all over the surface. We have chosen to present the HR-SEM investigations on S3 sample, as a clear evidence of gradient evolution with respect to EDX-STEM images shown in Figure 2 on S2 sample.

Indeed, the onset of materials clustering to form larger NPs starts with the smallest sizes shown by TEM for S1-S2, and is a clear confirmation of Oswald ripening mechanism [48], that is effective in many nanocomposite synthesis by additive deposition techniques, such as MAPLE.

~~Complementary understanding of coatings topography were achieved by analyzing the Atomic Force Microscopy images acquired on phenolic resin coatings, before carbonization (Figure S6 in the SI section). Data recorded on S3 coatings show that sub-micrometer sized clusters are uniformly dispersed all over the surface, in good agreement with the imagines recorded by HR-SEM presented in Figure 8. Also, particles size systematically increases from S1 to S5 due to higher salt precursor amount, in good agreement with previous TEM and EDX analyses on CoO NPs embedded in carbon matrix. Surface roughness also display a slight increase along the compositional gradient coatings due to higher cobalt nitrate salt amount.~~

4. Discussion

Porous carbon thin coatings embedded with CoO nanoparticles were synthesized by C-MAPLE technique in a gradient of composition and distinct size distributions. Several analytical tools were employed for composite materials characterization and revealed the influence of the laser processing approach (angular plume distribution) on the CoO NPs concentration and size distribution that governs gradient formation. In a previous study [30], we demonstrated the successful fabrication of porous carbon thin films by MAPLE and evidenced how solvents (chloroform, water, DMSO – 1:1 mixed with ethanol) used for targets preparation and the irradiation conditions (laser fluence) affect carbon coatings properties. It was shown that the coatings morphology and porosity could be tailored by the proper choice of the solvent, absorption of the laser wavelength and vapor pressure. We have chosen the ethanol-chloroform solvent mixture, because allowed us obtaining very uniform and porous carbon thin films with interconnected porous structures, displaying pore sizes between 10 to

15 nm [30]. On the other hand, Co doping of mesoporous carbon materials by LA-EISA as function of NPs precursor salts demonstrated the successful synthesis of functional magnetic materials [17]. The cobalt salts precursors (acetate, nitrate, and chloride) were shown to strongly influence the particles size and distribution but also carbon structural organization. Light-triggered small (3 ÷ 6 nm) and uniformly dispersed nanoparticles were obtained when using cobalt acetate and nitrate precursors, displaying super-paramagnetic properties. Cobalt chloride salt induced the formation of larger (~ 40 nm) and heterogeneously poly-dispersed NPs in the carbon matrix having ferromagnetic behavior.

Based on these premises, we advance with the present study a new approach for the fabrication of cobalt oxide-embedded mesoporous carbon coatings exhibiting a gradient of composition and different NPs sizes. ~~Uniformly distributed CoO NPs~~, High loading of 3 to 32 wt% of Co were measured on a 5 cm long C/CoO composites library, while particle sizes increase almost linearly from 3 to 8 nm. In addition, particle density is also changing with a 1:10 ratio leading to some particle aggregation. As expected, CoO NPs distribution seems to generate the formation of less ordered structures and decreased graphitization of carbon network, in agreement with previous studies [17]. Moreover, Co-NPs are oxidized as revealed by EDX, Raman spectroscopy and GIXRD patterns, due to low carbonization temperature and/or superficial oxidation because of air exposure [41,42,44,45]. The almost constant O amount in the coatings and the variation of carbon content suggest that functional oxygen groups are dominant in S1-S2 samples (high C *wt%* and low Co *wt%* and small NPs sizes), while on the opposite side of the coatings (samples S3-S5) oxygen is mainly bounded to metallic Co NPs. Moreover, we advanced ~~and confirm~~ the hypothesis of larger NPs formation by Oswald ripening mechanism [48], that should be taken into account in case of nanocomposite coatings synthesis by physical vapor deposition techniques.

The dynamics of plumes expansion is rather complex in case of MAPLE depositions. The condensation and clustering of the ablated materials and NPs formation was proven in case of Pulsed Laser Deposition [49,50]. In case of MAPLE, the mechanisms of the evaporated compounds expansion was addressed in molecular dynamics simulations by Leveugle and Zhigilei [51]. In another study [52], the same group have shown that an explosive ejection of the MAPLE target resulted in transfer of liquid micro-droplets with dimensions in the range of the optical penetration depth of the matrix, at the given wavelength. Both numerical and experimental studies devoted to MAPLE deposition of nanomaterials were reviewed by György and Caricato [53]. It is concluded that the appropriate choice of the deposition conditions could directly mediate the properties (size, geometry, composition and phase) of the MAPLE-transferred NPs. In our study, the metallic salt could agglomerate during the early stages of the quasi-adiabatic plume expansion by clustering and on the substrates surface during carbonization, in order to reach the thermodynamic equilibrium (e.g. the thermodynamically stable spherical shapes).

The mechanisms of MAPLE transfer, thin films growth and mesoporous carbon coatings synthesis were discussed before [30]. The addition of the metallic salt precursor during target preparation could lead to improved target absorption of the UV laser irradiation wavelength and increased deposition rate. Thus, one should adjust the irradiation parameters, for the fabrication of uniform layers while avoiding the excessive NPs agglomeration by choosing lower laser fluences. ~~Sub-micrometer sized salt clusters are visible in all of the AFM images on the surface of phenolic resins probably by crystallization during self-assembling process (Figure S6 in SI). Both the size and concentration of the salt structures increase by clustering, finally leading to larger CoO NPs embedded in the carbon framework.~~ It was previously reported that salts have a great influence on self-assembling, and thus the degree of carbon organization [12,54]. The gradient coatings are formed pulse-by-pulse by collecting the evaporated materials on the facing substrates. As a perspective, the synthesis of functional nanocomposite carbon coatings with pre-designed properties, could be achieved by the proper choice of the deposition conditions.

We emphasize that C-MAPLE is a versatile technique generally allowing a high degree of gradient control. First, the quantity of NPs could be easily tuned by modifying the initial quantity of the metallic salt precursor during target preparation. Thus, a calibration curve could be built after a dedicated parametric study, and quantitative elemental analyses of the coatings. Second, because C-MAPLE is an additive physical deposition technique, both particles size and density could be tailored by controlling the laser fluence and the number of applied laser pulses for targets evaporation. Indeed, for every fixed precursor salt concentration, various laser fluences and number of pulses could lead to distinct evaporation and deposition rates (nm/pulse). Third, the targets to substrates distance and separation between the laser spots on targets surface could strongly influence the spreading and intermixing of the evaporation plumes (angular distribution), leading thus to different blending of the materials and subsequent thin films growth. This could influence the NPs distribution (both the quantity and sizes) but also the properties of the carbon matrix. Fourth, because C-MAPLE is an additive deposition technique, a good control of coatings thickness is possible, and thus, allow the fabrication of composite coatings specifically designed for specific applications. Accordingly, one may easily fabricate low-doped thin coatings, high-doped thick ones, and combinations thereof by also modifying the NPs sizes as function of the envisaged properties. Moreover, C-MAPLE technique allows direct synthesis of adherent and cracks-free thin films on any kind of substrate, while the conventional synthesis methods (hard- and soft-template, EISA and LA-EISA) are more suited for materials synthesis as powders, subsequent steps being necessary to fabricate coatings for energy and/or catalysis applications.

Thus, the most promising perspectives that could be effectively explored for composite coating synthesis by C-MAPLE are: *i*) the use of other carbon and metal / metal oxide precursors in look of new properties and *ii*) the possibility of easy co-doping with two different materials in view of developing synergistic effects. MAPLE technique is suitable to address the synthesis of new hybrid materials and/or innovative properties for a broad spectrum of emerging applications while considering the performances *versus* fast, green and cost effective fabrication approaches.

4. Conclusions

We have proposed and validated a physical-chemical additive deposition technique for the fabrication of composite coatings with compositional gradient. It is demonstrated that combinatorial matrix-assisted pulsed laser evaporation followed by a thermal treatment can be successfully applied for the fast synthesis of cobalt oxide nanoparticles embedded in mesoporous carbon films exhibiting a gradient of composition and sizes. Our innovative laser approach is based on ~~controlled~~ evaporation and deposition of two cryogenic targets containing environmentally friendly organic carbon precursors and a metallic salt, and do not require any drying or thermo-polymerization prior the pyrolysis step, an advantage compared to classical techniques. It is shown that CoO NPs size and concentration increases along the substrates. CoO NPs size decreases from 8 nm on the highest concentration region to 3 nm at the furthest point of the substrates. The metal/metal oxides content could be rather accurately adjusted by the proper choice of the initial metallic salt quantity used for target preparation and irradiation conditions. ~~In the same time, CoO NPs size decreases from 8 nm on the highest concentration region to 3 nm at the furthest point of the substrates.~~

Acknowledgements

All authors acknowledge Bénédicte Réty for performing the thermal annealing treatments and Ludovic Josien for the HR-SEM analyses.

Funding: This work has been supported through the bilateral French-Romanian project SICABON (Partenariats Hubert Curien-Brancusi, RO-FR 9BM/2019). MS, CN, FJ, FS and

EA acknowledge the financial support from Romanian Ministry of Education and Research, under Romanian National Nucleu Programme LAPLAS VI – contract n. 16N/2019.

References

[1] C.M. Ghimbeu, M. Sopronyi, F. Sima, C. Vaulot, L. Vidal, J.-M. Le Meins, L. Delmotte, “Light-assisted evaporation induced self-assembly”: an efficient approach toward ordered carbon materials, Rsc Adv. 5 (2015) 2861–2868. https://doi.org/10.1039/c4ra14246b.

[2] T. Yang, J. Liu, R. Zhou, Z. Chen, H. Xu, S.Z. Qiao, M.J. Monteiro, N-doped mesoporous carbon spheres as the oxygen reduction reaction catalysts, J. Mater. Chem. A. 2 (2014) 18139–18146. https://doi.org/10.1039/c4ta04301d.

[3] N.A. Travlou, T.J. Bandosz, Nanoporous carbon-composites as gas sensors: Importance of the specific adsorption forces for ammonia sensing mechanism, Carbon. 121 (2017) 114–126. https://doi.org/10.1016/j.carbon.2017.05.081.

[4] K. Liu, J. Wang, T. Yang, H. Wang, C. Wang, M. Chen, An “in situ templating” strategy towards mesoporous carbon for high-rate supercapacitor and high-adsorption capacity on dye macromolecules, Carbon. 164 (2020) 19–27. https://doi.org/10.1016/j.carbon.2020.03.050.

[5] J. Song, T. Xu, M.L. Gordin, P. Zhu, D. Lv, Y.-B. Jiang, Y. Chen, Y. Duan, D. Wang, Nitrogen- Doped Mesoporous Carbon Promoted Chemical Adsorption of Sulfur and Fabrication of High- Areal- Capacity Sulfur Cathode with Exceptional Cycling Stability for Lithium- Sulfur Batteries, Adv. Funct. Mater. 24 (2014) 1243–1250. https://doi.org/10.1002/adfm.201302631.

[6] F. Li, Y. Wang, Z. Zhang, Y. Shen, S. Guo, A chemo/photo- co-therapeutic system for enhanced multidrug resistant cancer treatment using multifunctional mesoporous carbon nanoparticles coated with poly (curcumin-dithiodipropionic acid), Carbon. 122 (2017) 524–537. https://doi.org/10.1016/j.carbon.2017.07.008.

[7] H. He, L.A. Pham-Huy, P. Dramou, D. Xiao, P. Zuo, C. Pham-Huy, Carbon Nanotubes: Applications in Pharmacy and Medicine, Biomed Res. Int. 2013 (2013) 578290. https://doi.org/10.1155/2013/578290.

[8] T. Kyotani, N. Sonobe, A. Tomita, Formation of Highly Orientated Graphite from Polyacrylonitrile by Using a Two-Dimensional Space Between Montmorillonite Lamellae, Nature. 331 (1988) 331–333. https://doi.org/10.1038/331331a0.

[9] R. Ryoo, S.H. Joo, S. Jun, Synthesis of highly ordered carbon molecular sieves via template-mediated structural transformation, J. Phys. Chem. B. 103 (1999) 7743–7746. https://doi.org/10.1021/jp991673a.

[10] C.M. Ghimbeu, L. Vidal, L. Delmotte, J.-M. Le Meins, C. Vix-Guterl, Catalyst-free soft-template synthesis of ordered mesoporous carbon tailored using phloroglucinol/glyoxylic acid environmentally friendly precursors, Green Chem. 16 (2014) 3079–3088. https://doi.org/10.1039/c4gc00269e.

[11] J. Wang, C. Xue, Y. Lv, F. Zhang, B. Tu, D. Zhao, Kilogram-scale synthesis of ordered mesoporous carbons and their electrochemical performance, Carbon. 49 (2011) 4580–4588. https://doi.org/10.1016/j.carbon.2011.06.069.

[12] C.M. Ghimbeu, J.-M. Le Meins, C. Zlotea, L. Vidal, G. Schrodj, M. Latroche, C. Vix-Guterl, Controlled synthesis of NiCo nanoalloys embedded in ordered porous carbon by a novel soft-template strategy, Carbon. 67 (2014) 260–272. https://doi.org/10.1016/j.carbon.2013.09.089.

[13] H. Yu, W. Zhang, S. Miao, Y. Du, Y. Huang, D. Tang, Z.-A. Qiao, J. Wang, Z. Zhao, Synthesis of Co9S8 nanoparticle embedded, N, S Co-doped mesoporous carbon with salts as templates for electrocatalytic hydrogen evolution, Microporous Mesoporous Mater. 302 (2020) 110235. https://doi.org/10.1016/j.micromeso.2020.110235.

[14] D. Guo, Z. Tian, J. Wang, X. Ke, Y. Zhu, Co2N nanoparticles embedded N-doped mesoporous carbon as efficient electrocatalysts for oxygen reduction reaction, Appl. Surf. Sci. 473 (2019) 555–563. https://doi.org/10.1016/j.apsusc.2018.12.204.

[15] S. Abouali, M. Akbari Garakani, J.-K. Kim, Ultrafine SnO2 nanoparticles encapsulated in ordered mesoporous carbon framework for Li-ion battery anodes, Electrochimica Acta. 284 (2018) 436–443. https://doi.org/10.1016/j.electacta.2018.07.162.

[16] C. Nita, J. Fullenwarth, L. Monconduit, J.-M. Le Meins, J. Parmentier, M.T. Sougrati, C.M. Ghimbeu, Understanding the Sn Loading Impact on the Performance of Mesoporous Carbon/Sn-Based Nanocomposites in Li-Ion Batteries, Chemelectrochem. 5 (2018) 3249–3257. https://doi.org/10.1002/celc.201800835.

[17] C.M. Ghimbeu, M. Sopronyi, F. Sima, L. Delmotte, C. Vaulot, C. Zlotea, V. Paul-Boncour, J.-M. Le Meins, One-pot laser-assisted synthesis of porous carbon with embedded magnetic cobalt nanoparticles, Nanoscale. 7 (2015) 10111–10122. https://doi.org/10.1039/c5nr01687h.

[18] Y.-P. Zhu, Y. Liu, Y.-P. Liu, T.-Z. Ren, T. Chen, Z.-Y. Yuan, Direct Synthesis of Phosphorus-Doped Mesoporous Carbon Materials for Efficient Electrocatalytic Oxygen Reduction, Chemcatchem. 7 (2015) 2903–2909. https://doi.org/10.1002/cctc.201500148.

[19] X. Duan, S. Indrawirawan, H. Sun, S. Wang, Effects of nitrogen-, boron-, and phosphorus-doping or codoping on metal-free graphene catalysis, Catal. Today. 249 (2015) 184–191. https://doi.org/10.1016/j.cattod.2014.10.005.

[20] J. Wang, Y. Xia, Y. Liu, W. Li, D. Zhao, Mass production of large-pore phosphorus-doped mesoporous carbon for fast-rechargeable lithium-ion batteries, Energy Storage Mater. 22 (2019) 147–153. https://doi.org/10.1016/j.ensm.2019.01.008.

[21] B. Pan, X. Zhu, Y. Wu, T. Liu, X. Bi, K. Feng, N. Han, J. Zhong, J. Lu, Y. Li, Y. Li, Toward Highly Selective Electrochemical CO(2)Reduction using Metal-Free Heteroatom-Doped Carbon, Adv. Sci. 7 (2020) 2001002. https://doi.org/10.1002/advs.202001002.

[22] P. Hu, D. Meng, G. Ren, R. Yan, X. Peng, Nitrogen-doped mesoporous carbon thin film for binder-free supercapacitor, Appl. Mater. Today. 5 (2016) 1–8. https://doi.org/10.1016/j.apmt.2016.08.001.

[23] C. Nita, J. Fullenwarth, L. Monconduit, J.-M. Le Meins, P. Fioux, J. Parmentier, C.M. Ghimbeu, Eco-friendly synthesis of SiO2 nanoparticles confined in hard carbon: A promising material with unexpected mechanism for Li-ion batteries, Carbon. 143 (2019) 598–609. https://doi.org/10.1016/j.carbon.2018.11.069.

[24] C. Nita, J. Fullenwarth, L. Monconduit, L. Vidal, C.M. Ghimbeu, Influence of carbon characteristics on Sb/carbon nanocomposites formation and performances in Na-ion batteries, Mater. Today Energy. 13 (2019) 221–232. https://doi.org/10.1016/j.mtener.2019.05.009.

[25] L. Zhong, A. Chokkalingam, W.S. Cha, K.S. Lakhi, X. Su, G. Lawrence, A. Vinu, Pd nanoparticles embedded in mesoporous carbon: A highly efficient catalyst for Suzuki-Miyaura reaction, Catal. Today. 243 (2015) 195–198. https://doi.org/10.1016/j.cattod.2014.08.038.

[26] D. Saha, S. Deng, Hydrogen Adsorption on Ordered Mesoporous Carbons Doped with Pd, Pt, Ni, and Ru, Langmuir. 25 (2009) 12550–12560. https://doi.org/10.1021/la901749r.

[27] S. Li, Z. Lei, G. Yu, Q. Xu, W. Xu, R. Wu, M.K. Banks, Recycling the Catalyst of Atom Transfer Radical Polymerization to Prepare a Cu, N Codoped Mesoporous Carbon Electrocatalyst for Oxygen Reduction, Acs Sustain. Chem. Eng. 8 (2020) 12768–12774. https://doi.org/10.1021/acssuschemeng.0c00244.

[28] R. Sachse, D. Bernsmeier, R. Schmack, I. Haeusler, A. Hertwig, K. Kraffert, J. Nissen, R. Kraehnert, Colloidal bimetallic platinum-ruthenium nanoparticles in ordered mesoporous carbon films as highly active electrocatalysts for the hydrogen evolution reaction, Catal. Sci. Technol. 10 (2020) 2057–2068. https://doi.org/10.1039/c9cy02285f.

[29] E. Zagoraiou, N. Shroti, M.K. Daletou, Development of Pt-Co catalysts supported on carbon nanotubes using the polyol method-tuning the conditions for optimum properties,

Mater. Today Chem. 16 (2020) UNSP 100263. https://doi.org/10.1016/j.mtchem.2020.100263.

[30] E. Axente, M. Sopronyi, C.M. Ghimbeu, C. Nita, A. Airoudj, G. Schrodj, F. Sima, Matrix-Assisted Pulsed Laser Evaporation: A novel approach to design mesoporous carbon films, Carbon. 122 (2017) 484–495. https://doi.org/10.1016/j.carbon.2017.06.098.

[31] G. Ausanio, V. Califano, A. Costantini, G. Perretta, A. Aronne, G.P. Pepe, F. Sannino, L.R.M. Vicari, Matrix-assisted pulsed laser evaporation of β-glucosidase from a dopa/quinone target, Enzyme Microb. Technol. 132 (2020) 109414. https://doi.org/10.1016/j.enzmictec.2019.109414.

[32] S. Yang, J. Zhang, Deposition of YBCO nanoparticles on graphene nanosheets by using matrix-assisted pulsed laser evaporation, Opt. Laser Technol. 109 (2019) 465–469. https://doi.org/10.1016/j.optlastec.2018.08.039.

[33] A.D. Stiff-Roberts, W. Ge, Organic/hybrid thin films deposited by matrix-assisted pulsed laser evaporation (MAPLE), Appl. Phys. Rev. 4 (2017) 041303. https://doi.org/10.1063/1.5000509.

[34] L.E. Sima, G. Chiritoiu, I. Negut, V. Grumezescu, S. Orobeti, C.V.A. Munteanu, F. Sima, E. Axente, Functionalized Graphene Oxide Thin Films for Anti-tumor Drug Delivery to Melanoma Cells, Front. Chem. 8 (2020) 184. https://doi.org/10.3389/fchem.2020.00184.

[35] E. Axente, L. Elena Sima, F. Sima, Biomimetic Coatings Obtained by Combinatorial Laser Technologies, Coatings. 10 (2020) 463. https://doi.org/10.3390/coatings10050463.

[36] Scherrer Paul, Nachrichten von der Gesellschaft der Wissenschaften zu Göttingen, Math.-Phys. Kl. 2 (1918) 98–100.

[37] M. Enneiymy, P. Fioux, C.L. Drian, C.M. Ghimbeu, J.-M. Becht, Palladium nanoparticles embedded in mesoporous carbons as efficient, green and reusable catalysts for mild hydrogenations of nitroarenes, RSC Adv. 10 (2020) 36741–36750. https://doi.org/10.1039/D0RA05713D.

[38] A.C. Ferrari, Raman spectroscopy of graphene and graphite: Disorder, electron-phonon coupling, doping and nonadiabatic effects, Solid State Commun. 143 (2007) 47–57. https://doi.org/10.1016/j.ssc.2007.03.052.

[39] A.V. Ravindra, B.C. Behera, P. Padhan, Laser Induced Structural Phase Transformation of Cobalt Oxides Nanostructures, J. Nanosci. Nanotechnol. 14 (2014) 5591–5595. https://doi.org/10.1166/jnn.2014.9023.

[40] C.-W. Tang, C.-B. Wang, S.-H. Chien, Characterization of cobalt oxides studied by FT-IR, Raman, TPR and TG-MS, Thermochim. Acta. 473 (2008) 68–73. https://doi.org/10.1016/j.tca.2008.04.015.

[41] B. Liang, Y. Zhao, K. Li, C. Lv, Porous carbon codoped with inherent nitrogen and externally embedded cobalt nanoparticles as a high-performance cathode catalyst for microbial fuel cells, Appl. Surf. Sci. 505 (2020) 144547. https://doi.org/10.1016/j.apsusc.2019.144547.

[42] X. Li, C. Zeng, J. Jiang, L. Ai, Magnetic cobalt nanoparticles embedded in hierarchically porous nitrogen-doped carbon frameworks for highly efficient and well-recyclable catalysis, J. Mater. Chem. A. 4 (2016) 7476–7482. https://doi.org/10.1039/c6ta01054g.

[43] S. Grazulis, D. Chateigner, R.T. Downs, A.F.T. Yokochi, M. Quiros, L. Lutterotti, E. Manakova, J. Butkus, P. Moeck, A. Le Bail, Crystallography Open Database - an open-access collection of crystal structures, J. Appl. Crystallogr. 42 (2009) 726–729. https://doi.org/10.1107/S0021889809016690.

[44] J. Sanetuntikul, S. Hyun, P. Ganesan, S. Shanmugam, Cobalt and nitrogen co- doped hierarchically porous carbon nanostructure: a bifunctional electrocatalyst for oxygen reduction and evolution reactions, J. Mater. Chem. A. 6 (2018) 24078–24085. https://doi.org/10.1039/c8ta08476a.

[45] L. Zhou, J. Meng, P. Li, Z. Tao, L. Mai, J. Chen, Ultrasmall cobalt nanoparticles supported on nitrogen-doped porous carbon nanowires for hydrogen evolution from ammonia borane, Mater. Horiz. 4 (2017) 268–273. https://doi.org/10.1039/c6mh00534a.

[46] T. Roisnel, J. Rodriguez-Carvajal, WinPLOTR: A Windows tool for powder diffraction pattern analysis, 2001. https://doi.org/10.4028/www.scientific.net/MSF.378-381.118.

[47] Kourkoumelis Nikolaos, PowDLL, a reusable .NET component for interconverting powder diffraction data: Recent developments, ICDD Annu. Spring Meet. Ed Lisa ONeill Powder Diffr. 28 (2013) 137–148.

[48] H. Fischmeister, G. Grimvall, Ostwald Ripening — A Survey, in: G.C. Kuczynski (Ed.), Sinter. Relat. Phenom., Springer US, Boston, MA, 1973: pp. 119–149. https://doi.org/10.1007/978-1-4615-8999-0_9.

[49] D. Bäuerle, Laser Processing and Chemistry, Springer Science & Business Media, 2013.

[50] C.-Y. Shih, C. Wu, H. Wu, M. V. Shugaev, L. V. Zhigilei, Large-scale atomistic simulations of the generation of nanoparticles in short pulse laser ablation of metal targets: The effect of background gas and liquid environment, Chapter 12 in I.N. Mihailescu, A.P. Caricato, eds., Pulsed laser ablation: advances and applications in nanoparticles and nanostructuring thin films, Pan Stanford Publishing, Singapore, 2018.

[51] E. Leveugle, L.V. Zhigilei, Molecular dynamics simulation study of the ejection and transport of polymer molecules in matrix-assisted pulsed laser evaporation, J. Appl. Phys. 102 (2007) 074914. https://doi.org/10.1063/1.2783898.

[52] E. Leveugle, A. Sellinger, J.M. Fitz-Gerald, L.V. Zhigilei, Making molecular balloons in laser-induced explosive boiling of polymer solutions, Phys. Rev. Lett. 98 (2007) 216101. https://doi.org/10.1103/PhysRevLett.98.216101.

[53] E. György and A. P. Caricato, MAPLE Deposition of Nanomaterials, Chapter 6 in I.N. Mihailescu, A.P. Caricato, eds., Pulsed laser ablation: advances and applications in nanoparticles and nanostructuring thin films, Pan Stanford Publishing, Singapore, 2018.

[54] S. Sun, C.M. Ghimbeu, R. Janot, J.-M. Le Meins, A. Cassel, C. Davoisne, C. Masquelier, C. Vix-Guterl, One-pot synthesis of LiFePO4-carbon mesoporous composites for Li-ion batteries, Microporous Mesoporous Mater. 198 (2014) 175–184. https://doi.org/10.1016/j.micromeso.2014.07.039.

Table I. Evaluation of the average C, O, and Co quantity within gradient mesoporous composite coatings.

Sample / Average quantity (*wt%*)	**Co**	**C**	**O**
S1	3.46(0.05)	90.7(2)	5.82(6)
S2	5.48(0.05)	89.0(1)	5.52(4)
S3	10.00(0.07)	85.0(1)	5.00(4)
S4	20.02(0.12)	72.22(2)	7.76(7)
S5	32.43(0.16)	62.5(2)	5.01(4)

Values in parenthesis represents the estimated standard deviation (e.s.d.) associated to the main value, i.e. 3.46(5) means 3.46±0.05.

Table II. Main results for (200) reflection individual profile fitting: peak intensity, FWHM and evaluation of the coherent domains size. The average CoO NPs size and the number of counted particles ~~their population density after~~ based on TEM images analyses are presented in the last two columns.

Sample	**(200) diffraction peak intensity (cps)**	**FWHM for (200) diffraction peak (°2θ)**	**Coherent domains sizes[1] (Scherrer [40]) (nm)**	**Average CoO NPs size~~*~~[3] (nm)**	**Counted CoO NPs~~*~~[3]**
S1	n/a	n/a	n/a	2.81 (3)	276
S2	n/a	n/a	n/a	3.17 (3)	799
S3	27(8)	3(2)	2.6 (1.5 ÷ 8.3)[2]	6.10 (7)	1074
S4	30(4)	1.1(4)	8 (5.8 ÷ 12.8)[2]	7.08 (5)	2080
S5	34(3)	0.9(1)	9.6 (8.3 ÷ 11.5)[2]	7.45 (7)	2751

Values in parenthesis represents the estimated standard deviation, except for those marked [2],
(1): Assuming that only size effects are responsible for the widening of reflections, or are preponderant.
~~*(2): Taking into account the error on the FWHM and on the line position.*~~
~~**determined by TEM analyses.*~~
(2): Taking into account the error on the FWHM and on the line position, data in parenthesis give the minimum and maximum values for the coherent domain size.
(3): Determined by TEM and particles size distribution profile analyses.

Figure captions:

Figure1. Global view of C-MAPLE deposition experimental setup (a); detailed scheme of targets - substrates arrangement (b).

Figure 2. EDX mapping of C, Co, and O distribution within coatings acquired on sample S2. The left top image represents the STEM image of the material indicating the zone where the EDX was performed. Scale bar is 100 nm in all images.

Figure 3. EDX analysis on the evolution of C, Co and O mass fractions along the compositional gradient for the S1- S5 samples. The solid curves represent the linear fitting of data in case of O and second degree polynomial fitting for Co and C concentrations respectively.

Figure 4. Raman spectra of the CoO-embedded mesoporous carbon compositional gradient coatings (a). Inset table shows the I_D/I_G ratio calculated by using the areas under the peaks after spectra deconvolution and peaks normalization to G band. The evolution of the peaks corresponding to CoO in S1-S5 samples (b).

Figure 5. GI-XRD (αi=1°) patterns of CoO-embedded mesoporous carbon compositional gradient coatings (a). (200) individual profile refinement approach on S5 (b).

Figure 6. TEM images (100 and 50 nm scales) of S1-S5 C-MAPLE samples and the corresponding analyses of NPs size and density distribution, within carbon matrix. Experimental size distribution is better refined with a lognormal function (solid line) for each sample. (1): most frequent size, (2): total number of particles counted. CoO NPs size increases from a) to e).

Figure 7: Selected area electron diffraction of S2 (a) and S5 (b) materials.

Figure 8. Most common CoO particle size determined by TEM versus cobalt weight percent resulted from EDX analyses for each S1-S5 sample. The red curve represents the exponential fitting of data.

Figure 9. HR-SEM morphological investigations of sample S3. A higher magnification image is introduced to evidence clusters formation. Scale bars are 1 µm in both images.

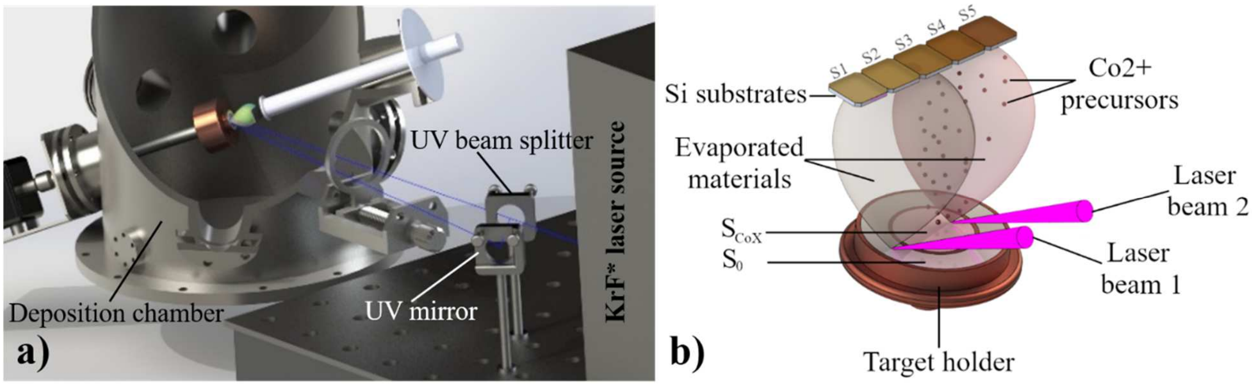
UV beam splitter
KrF* laser source
Deposition chamber
UV mirror
a)
S1
S2
S3
S4
S5
Si substrates
Co2+ precursors
Evaporated materials
Laser beam 2
S_CoX
S_0
Laser beam 1
Target holder
b)

Figure 1.

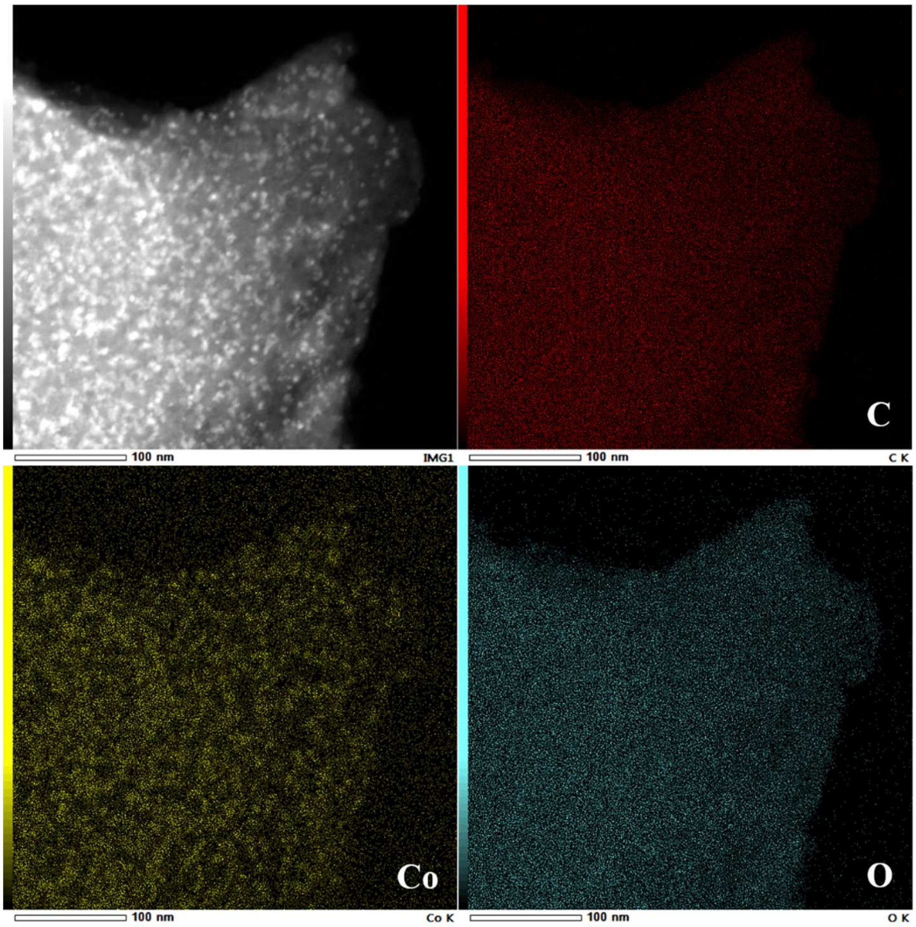

Figure 2.

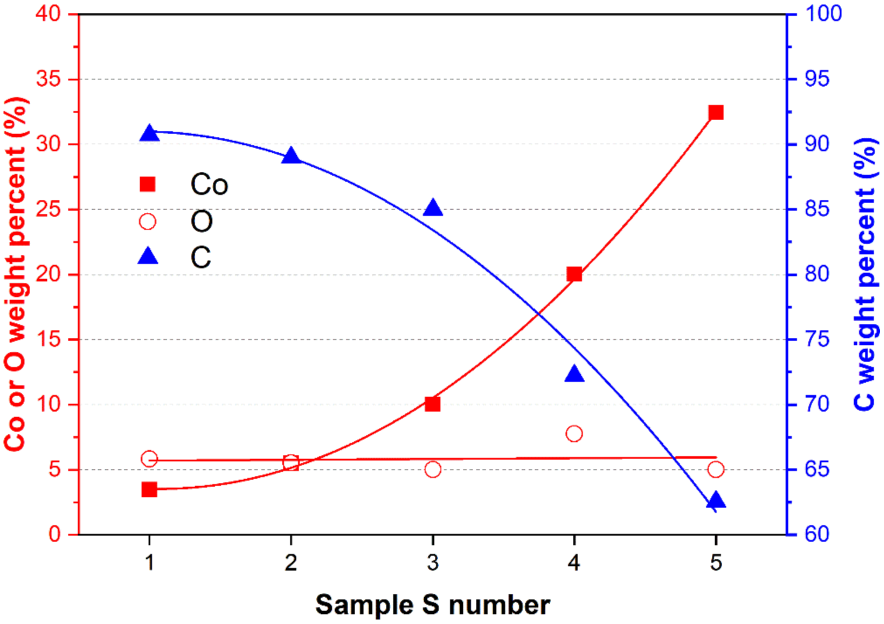
Co or O weight percent (%)
0
5
10
15
20
25
30
35
40
C weight percent (%)
60
65
70
75
80
85
90
95
100
Sample S number
1
2
3
4
5
Co
O
C

Figure 3.

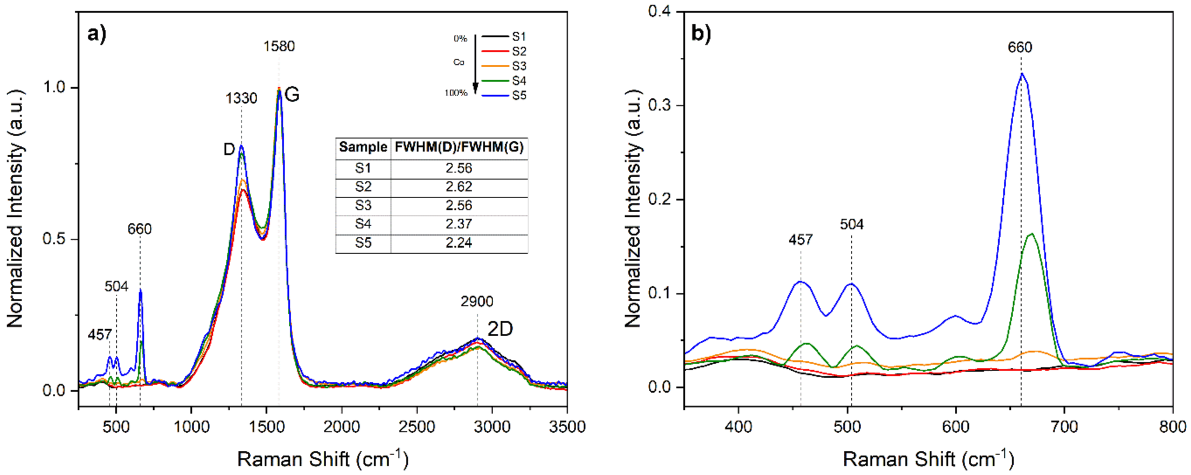

Sample	FWHM(D)/FWHM(G)
S1	2.56
S2	2.62
S3	2.56
S4	2.37
S5	2.24

Figure 4.

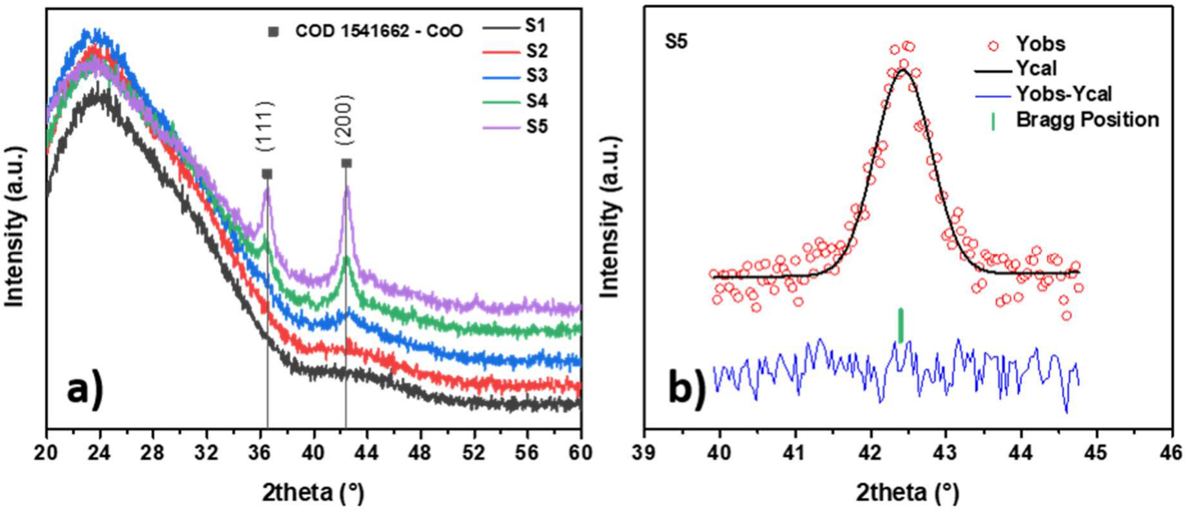
a)
COD 1541662 - CoO
S1
S2
S3
S4
S5
(111)
(200)
Intensity (a.u.)
2theta (°)
20
24
28
32
36
40
44
48
52
56
60
b)
S5
Yobs
Ycal
Yobs-Ycal
Bragg Position
Intensity (a.u.)
2theta (°)
39
40
41
42
43
44
45
46

Figure 5.

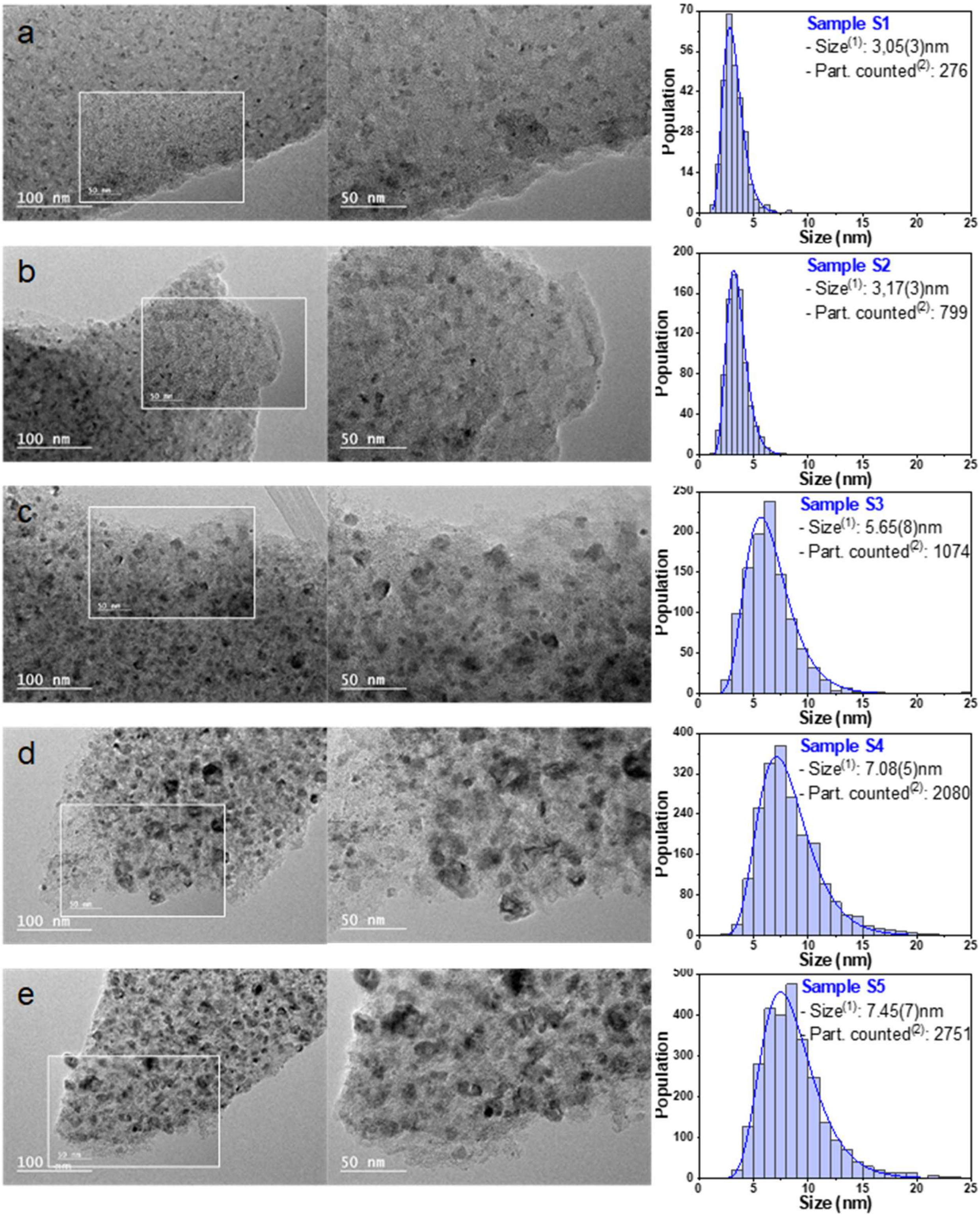
a
b
c
d
e
100 nm
50 nm
Sample S1
- Size(1): 3,05(3)nm
- Part. counted(2): 276
Sample S2
- Size(1): 3,17(3)nm
- Part. counted(2): 799
Sample S3
- Size(1): 5.65(8)nm
- Part. counted(2): 1074
Sample S4
- Size(1): 7.08(5)nm
- Part. counted(2): 2080
Sample S5
- Size(1): 7.45(7)nm
- Part. counted(2): 2751
Population
Size (nm)
0
5
10
15
20
25

Figure 6.

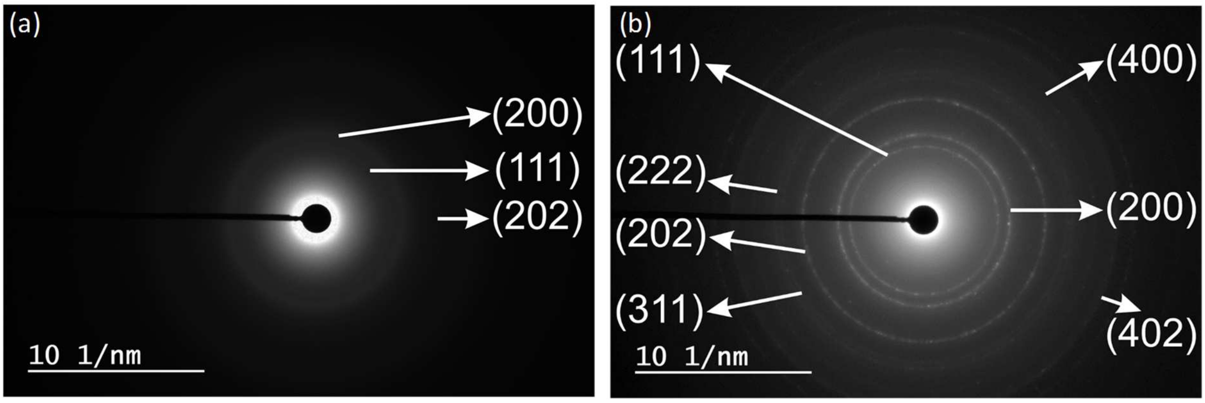

Figure 7.

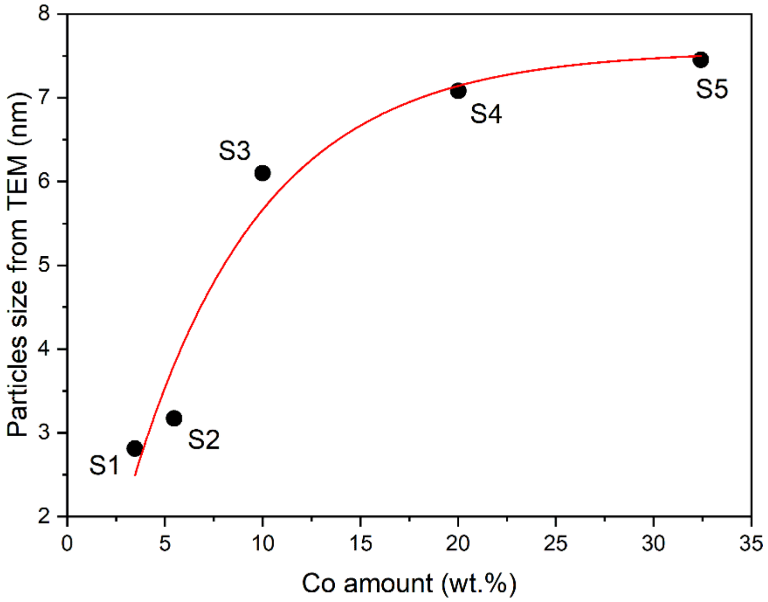
Particles size from TEM (nm)
8
7
6
5
4
3
2
0
5
10
15
20
25
30
35
Co amount (wt.%)
S1
S2
S3
S4
S5

Figure 8.

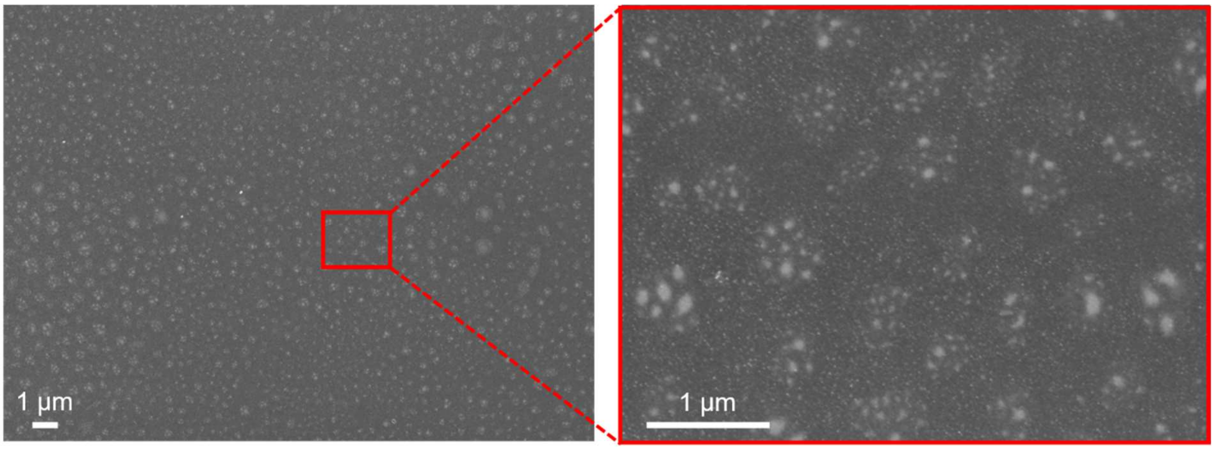

Figure 9.

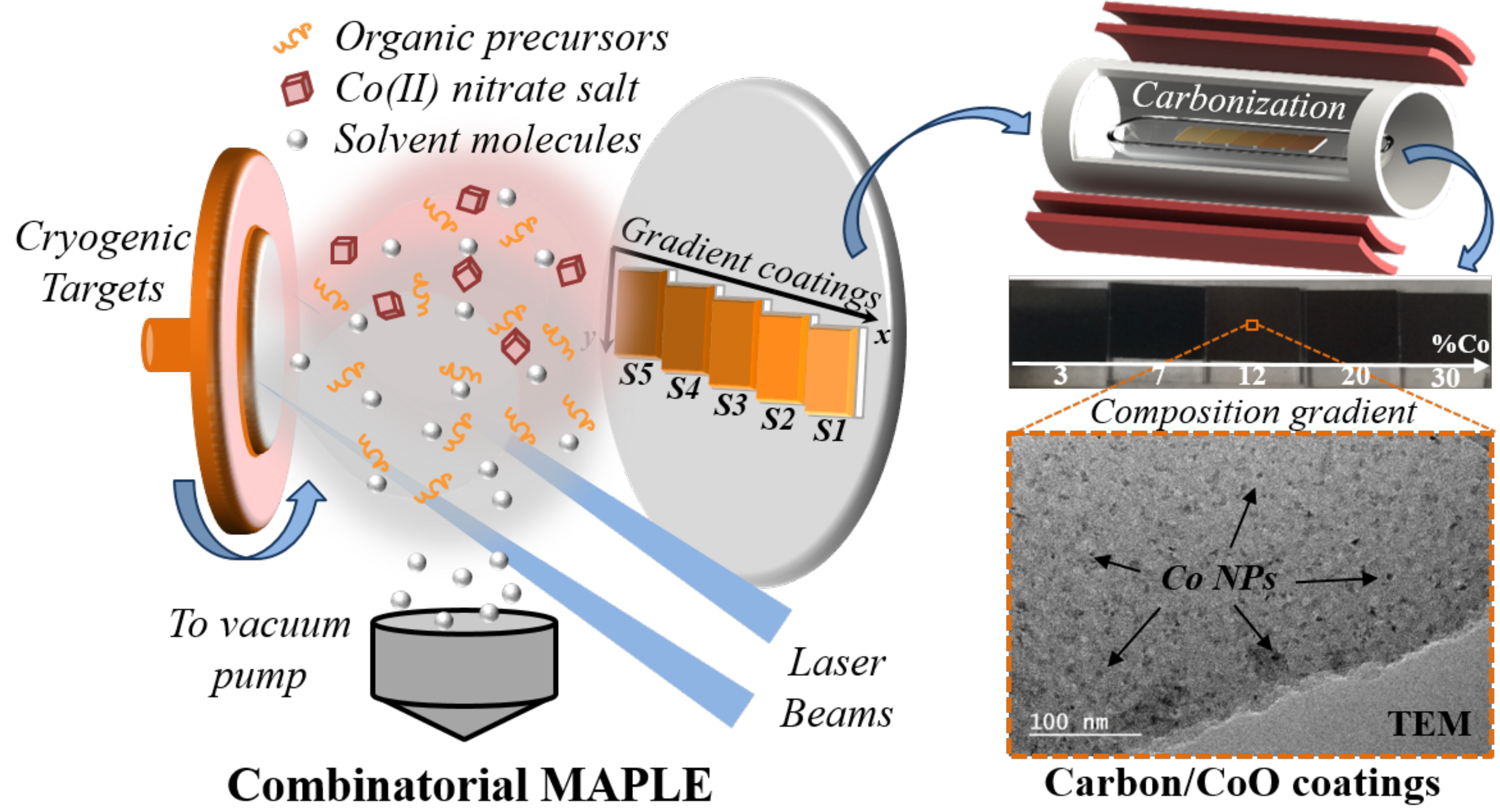
Organic precursors
Co(II) nitrate salt
Solvent molecules
Cryogenic Targets
Gradient coatings
x
y
S5
S4
S3
S2
S1
To vacuum pump
Laser Beams
Combinatorial MAPLE
Carbonization
%Co
3
7
12
20
30
Composition gradient
Co NPs
100 nm
TEM
Carbon/CoO coatings